Tunnelling and Underground Space Technology 81 (2018) 26–34

Contents lists available at ScienceDirect

Tunnelling and Underground Space Technology

journal homepage: www.elsevier.com/locate/tust

Understanding progressive rock failure and associated seismicity using ultrasonic tomography and numerical simulation

Tai-Ming He[a], Qi Zhao[b,*], Johnson Ha[b], Kaiwen Xia[b], Giovanni Grasselli[b]

[a] Key Laboratory of Seismic Observation and Geophysical Imaging, Institute of Geophysics, China Earthquake Administration, Beijing 100081, China
[b] Department of Civil and Mineral Engineering, University of Toronto, ON M5S 1A4, Canada

ARTICLE INFO

Keywords:
Ultrasonic tomography
FDEM
AE
b-value
Precursors

ABSTRACT

Monitoring the stability of underground rock excavation zones, such as tunnels and underground mines, is critical to their operational safety. The stability of these structures is related to the stress redistribution introduced by the excavation process and disturbance during the operation. Therefore, the characteristics of progressive rock failure behaviour at different stress conditions must be investigated. In this study, we address this problem using a laboratory experiment, coupled with ultrasonic tomography (UT) and numerical simulation. A time-lapse two-dimensional (2D) UT observation was conducted on a granite slab under uniaxial compression. This test was then reproduced numerically by the combined finite-discrete element method (FDEM). This innovative combination of technologies depicted the entire deformation and failure processes at macroscopic and microscopic scales. Quantitative assessments of the results suggested six precursory behaviours indicating the catastrophic failure of the rock: (1) decrease of the average wave velocity perpendicular to the loading direction, (2) increase of the heterogeneity and anisotropy of wave velocity, (3) exponential increase of seismic rate, (4) spatial localization of damage onto the failure plane, (5) increase of the dominance of shear failure, and (6) slight recovery of b-value, followed by a significant drop. An integrated monitoring and analysis of these indicators, accompanied by carefully calibrated numerical simulations, may provide vital information regarding the stability of underground structures.

1. Introduction

Many tunnels and underground structures are constructed through highly stressed brittle rocks. Under high-stress conditions, stress redistribution occurs during and after the excavation which generates energy imbalance in the rock mass. The resultant formation, propagation, and coalescence of microcracks alter the properties of the surrounding rock mass and impact the stability of underground structures (Chang and Lee, 2004). Therefore, fundamental studies evaluating the failure and damage mechanisms of rock at different stress states are of great importance to geo-hazard assessment and operational safety of underground structures.

Under this motivation, we conducted a time-lapse ultrasonic tomography (UT) observation on a granite slab subjected to a uniaxial compression test. UT has been used in medical science since the seventies (Greenleaf et al., 1974), but was only in the eighties that Neumann-Denzau and Behrens (1984) applied this technology to rocks. UT utilizes ultrasonic wave signals (> 20 kHz) to penetrate the sample and image the velocity structure of the sample interior (i.e. tomography). Due to the high scattering and attenuation nature of the ultrasonic wave, UT is typically used for laboratory and small-scale field applications. For example, UT was used by Falls et al. (1992) to investigate micromechanical response of the rock due to hydraulic fracturing in laboratory experiments; Jansen et al. (1993) used UT to monitor and study thermally induced damage in granite in laboratory scale tests; and Meglis et al. (2005) used UT to assess in situ microcrack damage during excavation process of a tunnel.

Ultrasonic wave velocity is influenced by a number of factors including: pressure, crack density and orientation, and pore fluid properties (Johnston and Toksöz, 1980; Lockner et al., 1977; Sayers and Kachanov, 1995; Stanchits et al., 2006). Extracting information regarding such factors from elastic wave velocity using tomography provides a non-destructive approach to study the rock interior and is ideal to study the property changes of the rock during compression tests (Paterson and Wong, 2005). Thus, we conducted a uniaxial compression test on a granite slab and used UT to investigate the progressive failure process of the sample.

On the other hand, micromechanics based numerical simulations

* Corresponding author.
E-mail address: q.zhao@mail.utoronto.ca (Q. Zhao).

https://doi.org/10.1016/j.tust.2018.06.022
Received 10 May 2017; Received in revised form 29 April 2018; Accepted 26 June 2018
Available online 04 July 2018

have been used to improve the understanding of laboratory experiments. For example, Zhu and Tang (2004) used the Rock Failure Process Analysis Code (RFPA) to investigate the deformation and failure process of heterogeneous rock at the mesoscopic level. Mahabadi et al. (2014, 2012b) used the Y-Geo code to study microscale heterogeneity and microcracks on the failure behaviour and mechanical response of crystalline rocks. Hengxing et al. (2010) used grain-based Universal Distinct Element Code (UDEC) to simulate the role of micro-heterogeneity in controlling the micromechanical behaviour and the macroscopic response of granite when subjected to uniaxial compression loading. Hazzard et al. (2000) used Particle Flow Code (PFC) to examine crack nucleation and propagation in brittle rocks and the associated energy release.

In order to improve our understanding of the laboratory observations, we used the two-dimensional (2D) combined finite-discrete element method (FDEM) to numerically reproduce the uniaxial compression test. The FDEM model synthesizes the macroscopic behaviour of materials from the interaction of micro-mechanical constituents and provides insights into the failure processes of rocks from elastic and inelastic deformation to fracturing (Mahabadi et al., 2012a; Munjiza, 2004). FDEM was also used to simulate acoustic emission and microseismic activity (Lisjak et al., 2013; Zhao, 2017; Zhao et al., 2015, 2014).

The innovative combination of UT observations and FDEM simulations allowed us to characterize the deformation and brittle failure processes of the rock at macroscopic and microscopic scales. We quantitatively analysed the velocity anisotropy and statistical characteristics of simulated acoustic emission (AE). These results provided detailed information on the damage evolution in the rock and the variation of velocity anisotropy. Six evident precursors of the rock failure were identified, and by comparing with laboratory tests, field observations, and numerical simulations reported in the literature, we can infer that these precursors, which can also be obtained from field seismic monitoring, may provide information for forecast and mitigate rock mass catastrophic failure.

2. Material and methods

2.1. Material and experiment set-up

The rock sample investigated in this study is a Fangshan granite slab 110 mm wide, 220 mm long, and 30 mm thick. Fangshan granite is a coarse grain rock consisting of three main mineral phases: feldspar, quartz, and biotite, with an average grain size of 2.6 mm. A uniaxial compression test was conducted on this sample using an MTS–1000KN hydraulic test system (Fig. 1a), which is able to control the axial load with less than 0.5% error. During the compression test, the axial load was increased at a rate of 6 kN/min (~1.82 MPa/min). At the initial (i.e. 0 MPa), and every 20 MPa incremental stress level, a UT test was performed.

2.2. Ultrasonic tomography (UT)

The UT system used in this study consists of five main components (Fig. 1):

(1) Ultrasonic transducers. Two types of transducers were used in this study, Physical Acoustics Corporation (PAC) Nano-30 and Valpey-Fisher Pinducer model VP1093. The PAC Nano-30 transmitter has a bandwidth of 125–750 kHz, while the VP1093 transmitter has a bandwidth of 10–10,000 kHz. The mixed usage of transducers was due to the limited number of either type in our lab; however, as received signals showed no significant quality difference between the two types, we did not consider the error associated with the differences in used transducers. Ten transducers were placed on the left and right sides of the slab, with 20 mm vertical spacing, and three transducers were placed at the middle of the top and bottom sides of the slab, with 25 mm lateral spacing (Fig. 2a and b). These transducers were coupled to the sample using epoxy. Transducers on the top and bottom sides of the sample were embedded in specially designed slots on the loading platens.
(2) An ultrasonic waveform generator (National Instrument NI–5421). The NI–5421 device, which was configured with the PXI-100B chassis, has a frequency range from < 1 mHz to 43 MHz. We used a computer to control a digital to analogue channel of this device to generate a square wave signal at 1 MHz with a peak-to-peak voltage of 1 V, which was then amplified by an amplifier (Pintek HA–405) to 100 V.
(3) A custom multi-channel switch was used to replicate multiple identical ultrasonic signal traces from the amplified signal.
(4) A custom ultrasonic switchbox, operated by an NI–2567 device (not shown in the figure). The ultrasonic switchbox was used for switching sensors between transmitting signal and receiving signal during the experiment. Each UT test consisted of four stages, and during each stage, transducers on one side of the sample acted as transmitters while transducers on the other three sides acted as receivers. This operation started from the left side (i.e. transducers 1–10) and carried on counterclockwise (Fig. 2b).
(5) A 32-channel data acquisition system, which consists of 16 PAC PCI-2 boards. This system can acquire analogue signals from the transducers, convert them to digital signals and transmit them to the computer. The wave velocity between a source and receiver transducer pair can be directly estimated using the source-receiver distance divided by the travel time. This velocity is the result of the effects of the media along the wave path (i.e. raypath), and it only indicates the overall variation of velocity. In the following discussions, we refer to it as averaged velocity (v_a). We calculated the averaged P-wave velocities between transducer pairs perpendicular ($v_a^{\perp}$) and parallel ($v_a^{\parallel}$) to the loading direction and examine their variations against the stress condition. Note that at high stress levels, transducers 11 and 13 were loosely coupled due to sample deformation. In order to study $v_a^{\parallel}$ under high stress, we examined v_a between transducer 12 and transducers 24, 25, and 26.

In order to obtain the spatial variation of wave velocity in the rock, inversion of the velocity taking into consideration the rock heterogeneity (i.e. tomography) was required (Aki and Lee, 1976). Tomography was performed on grids with a grid cell size of 10 mm × 10 mm, resulting in a 2D velocity map of the sample. The raypath lengths were estimated using a wave front ray-tracing technique, and the damped least square (LSQR) iterative inversion method was applied, using a damping factor of 10, with 20 iterations (Paige and Saunders, 1982; Zhao et al., 1992). To obtain the initial velocity values of the iterative inversion, a linear fit of travel time and the travel distances between all source-receiver pairs at each stress level was carried out, and the slope of this fitted curve was used as the initial value in the inversion. Moreover, to constrain the inversion, the velocity of each grid was limited to the range of 3500–5500 m/s.

2.3. Combined finite-discrete element method (FDEM)

The FDEM model consisted of a 220 mm × 110 mm longitudinal section representing the rock sample and two rectangles at the top and bottom of the rock sample representing the loading platens. The model was discretized using a finite-element mesh with an average element size comparable to the rock sample grain size (i.e. 2.6 mm). The model recreated the Fangshan granite sample that the mineral phases were represented by approximately 10,000 elastic triangular elements connected to each other by four-node cohesive crack elements (CCEs) that represent grain boundaries. These CCEs can deform elastically, yield, and break according to the principles of non-linear elastic fracture mechanics, which allows FDEM models to capture the deformation and

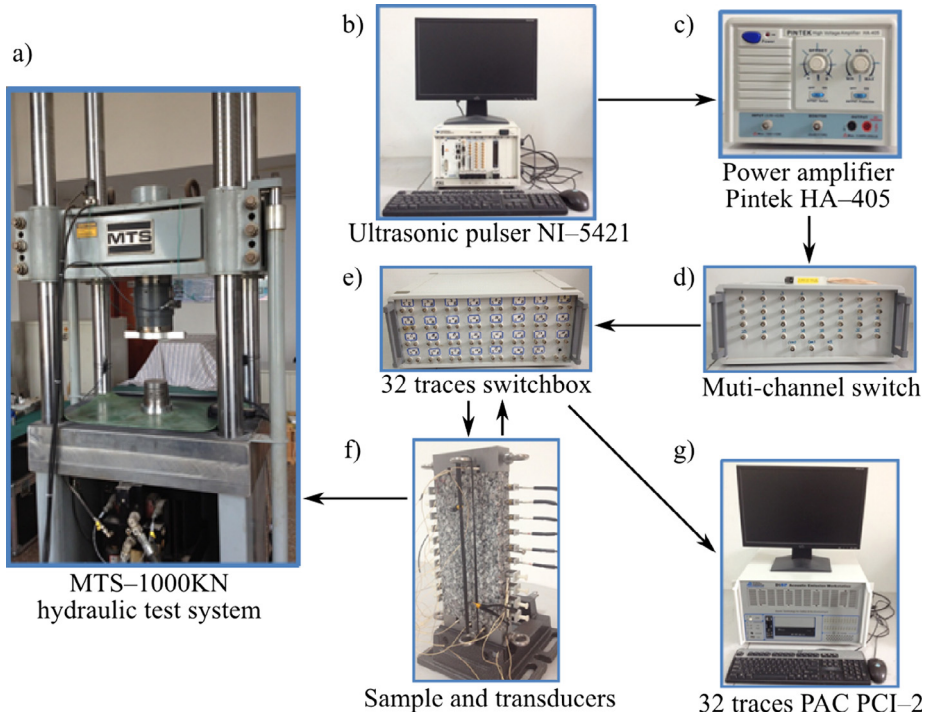

Fig. 1. Illustration of the experiment set-up. (a) The MTS–1000KN test system, (b) the computer controlled ultrasonic pulser, (c) power amplifier, (d) multi-channel switch, (e) the 32 traces switchbox, (f) the sample with transducers attached on it, and (g) the 32 traces PAC-PCI–2 data acquisition device.

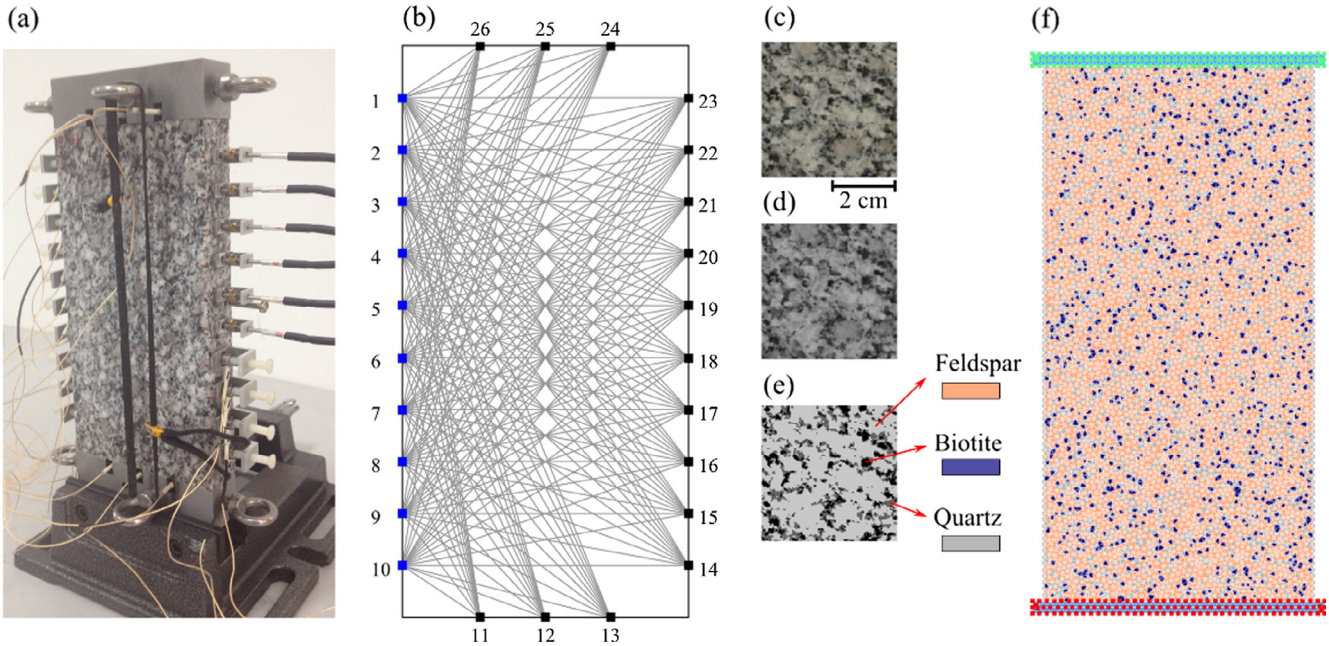

Fig. 2. (a) Ultrasonic signal transducers attached to the sides of the specimen. (b) Schematic diagram of the raypath at the first stage of the UT test. Transducers 18–23 are VP1093 and the others are Nano-30. (c)–(e) Procedure of estimating the relative abundance of minerals in the rock specimen. (f) FDEM model of the rock specimen.

fracturing behaviour of solids by modelling the entire failure path (Barenblatt, 1962; Dugdale, 1960; Mahabadi et al., 2012a; Munjiza, 2004). The breakage of CCEs can occur in tensile mode (mode I), shear mode (mode II) or a combination of the two (mixed mode), based on user defined energy based thresholds that are calibrated to match laboratory test results (Tatone and Grasselli, 2015).

In order to incorporate the heterogeneity of the Fangshan granite in the model, the relative percentage of the three major mineral phases were estimated by employing an image based analysis approach and then assigned to the model. A photograph of the specimen was taken (Fig. 2c) and converted to an 8-bit grayscale image (Fig. 2d). A segmentation process based on visual inspection of grayscale values of different minerals was carried out: greyscale values > 100 and < 68 were considered feldspar and biotite, respectively, while the remaining mineral phases were considered quartz (Fig. 2e). The segmentation showed that the Fangshan granite sample consists of 67% feldspar, 23% quartz and 10% biotite. Elements in the FDEM model were assigned according to such percentages with stochastic spatial distribution

Table 1
Mineral properties and intergranular boundary properties used in the FDEM model for the Fangshan granite sample, adapted from Mavko et al. (1998) and Lisjak et al. (2013).

Mineral property (unit)	Feldspar	Quartz	Biotite
Volume fraction (%)	67	23	10
Density (kg·m^{-3})	2600	2600	2800
Young's modulus (GPa)	56.4	83.1	17.2
Poisson's ratio (–)	0.32	0.07	0.36
Internal friction coefficient (–)	1.27	1.27	1.27
Internal cohesion (MPa)	37	37	37
Tensile strength (MPa)	5.5	11.4	4.2
Mode I fracture energy (J·m^{-2})	310	907	599
Mode II fracture energy (J·m^{-2})	620	1812	1198
Intergranular boundary property (unit)	Feldspar-quartz	Feldspar-biotite	Quartz-biotite
Friction coefficient (–)	0.82	0.82	0.82
Cohesion (MPa)	37	37	37
Tensile strength (MPa)	0.235	0.235	0.235
Mode I fracture energy (J·m^{-2})	0.6	0.05	0.05
Mode II fracture energy (J·m^{-2})	1450	382	382

(Fig. 2f). Properties of minerals and boundaries between different minerals (intergranular boundaries) were assigned using typical values from the literature and fine-tuned to match the laboratory results (Table 1).

Two loading platens were assumed to be rigid and they loaded the sample at a constant velocity of 0.2 m·s^{-1}, which corresponds to a strain rate of 0.91 s^{-1}. The loading rate, although significantly higher than in the actual test, has been verified to ensure a quasi-static loading condition while allowing the simulation to run in a reasonable time (Mahabadi, 2012; Tatone and Grasselli, 2015). In order to reproduce the effect of the friction between the platens and the rock, a friction coefficient of 0.2 was assigned to the interfaces between them. The software package Irazu 2.0.0 (Geomechanica Inc.) was used to build the model and run the simulation.

2.4. Simulated acoustic emission (AE)

Energy release event associated with the microscopic cracking process in the rock is usually referred to as acoustic emission (AE) (Lockner, 1993). Understanding AE activities can help us link microscopic damage to observed macroscopic behaviour of the rock sample, and it has been commonly used together with UT to understand rock damage (Falls and Young, 1998; Stanchits et al., 2006).

In this study, AE activities during the laboratory compression test were considered noise as they interfered the UT signals, and they were not analysed. Combining UT and AE monitoring during the loading process is challenging because of the significant differences between the two types of signals (Falls et al., 1992). Accomplishing such a functionality may require two instrumentation systems (Jansen et al., 1993), which is beyond the capability of the current set-up. On the other hand, Lisjak et al. (2013) implemented an AE simulation algorithm in FDEM that considered each breakage of a CCE as an AE. Occurrence time, kinetic energy release, coordinates, and failure mode of each AE are recorded. This method captures the event information at the source location based on the deformation and failure of CCEs; thus, bypassing the complexity of inversion process that is required for conventional AE monitoring techniques used in the lab. This method was used to simulate AE at different stress conditions and microseismic events in hydraulic fracturing operations, which demonstrated similar magnitude range and statistical characteristics to laboratory and field observations (Lisjak et al., 2013; Zhao et al., 2014). In this works, using this AE simulation method and the calibrated model, we investigated damage process in the rock by quantitatively studying simulated AE.

Similar to the UT observation, we have examined AE between stress points at each 20 MPa interval; additionally, the peak stress point was also taken into consideration. The AE count in each interval was associated with the correspondent stress-strain behaviour. The failure mode and spatial density of simulated AE pre- and post-peak were studied based on a grid with a grid cell size of 5 mm × 5 mm.

The distribution of AE in the magnitude domain, that is, the frequency magnitude distribution (FMD), was examined using the b-value in the Gutenberg-Richter (G-R) law (Gutenberg and Richter, 1944). Variation of b-value provides important information regarding the earthquake source region. In order to study the evolution of the characteristics of b-value during the deformation and failure process, we evaluated temporal variation of b-value with a sliding time window method (Nuannin and Kulhanek, 2005). This method examines AE in a time window that contains N AE events, and the window slides through the AE catalogue in a timely order by increments of s event counts. In this study, we chose $N = 200$ as the window size and $s = 20$ (i.e. $s = N/10$) as the incremental step size. b-value within each window was calculated using the maximum likelihood method (Aki, 1965; Bender, 1983), with a bin size of 0.1 unit magnitude. The magnitude of completeness (M_c), which is the cut-off magnitude below which events are not considered into the b-value estimation, was obtained by applying the maximum curvature method to the complete AE catalogue (Wiemer and Wyss, 2000). The error associated with b-value was estimated using a bootstrap approach (Efron and Tibshirani, 1986; Zhao et al., 2015).

3. Results

3.1. Compression test results

The Fangshan granite sample had a uniaxial compression strength (σ_c) of 136 MPa, a Young's modulus (E) of 57 GPa, and a Poisson's ratio (υ) of 0.20. These results, as well as the fracture pattern of the failed laboratory sample, were used to calibrate the FDEM model. The calibrated simulation resulted in emergent σ_c, E, and υ values of 138 MPa, 61 GPa, and 0.21, respectively. These values matched well with the respective experimental values.

The stress-strain relation from the laboratory test was not linear at the initial portion (i.e. 0–30 MPa), which was related to the closure of microcracks in the sample. However, the influence of microcracks was not considered in the FDEM modelling and the initial portion of the stress-strain curve was linear, which resulted in a difference in strain of approximately 0.02% (Fig. 3). On the other hand, the rock sample failed abruptly at peak stress during the laboratory test, and the test was stopped at this point. This abrupt failure was reproduced in the simulation where the stress dropped immediately after the peak stress; however, the simulation was stopped shortly after the peak stress point, when a catastrophic macroscopic failure occurred.

3.2. Tomography results

The recorded waveforms showed that as the rock deformed with increasing stress, signal to noise ratio decreased, which may be related to (i) the flawed coupling between transducers and the sample and (ii) increased AE activities (Fig. 4). Automated arrival picking techniques could not consistently detect arrivals and waveforms of waves, especially at high stress levels. Therefore, hand-picked arrivals of P-waves were used for tomography analysis in this study.

The averaged velocity perpendicular to the loading direction, $v_a^{\perp}$, calculated from all transducer pairs across the sample laterally increased when the axial stress increased from 0 to 60 MPa (Fig. 5). After 60 MPa, $v_a^{\perp}$ tended to decrease, reaching values lower than the initial

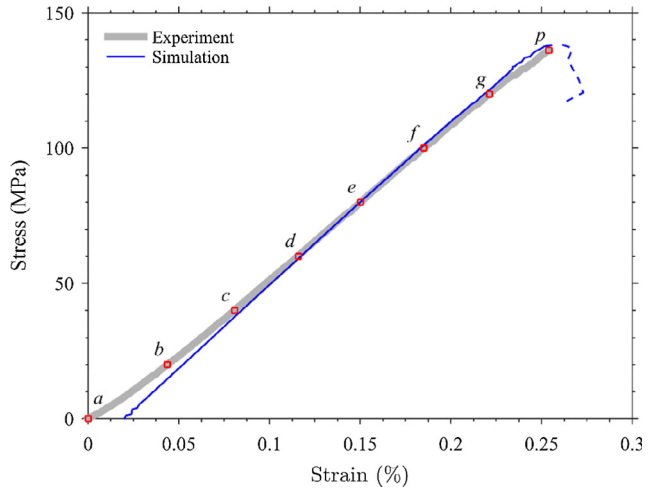

Fig. 3. Stress-strain behaviour of the tested Fangshan granite (thick grey curve) and the FDEM simulation result (thin blue curve). The simulated strain is shifted to the positive strain direction by 0.02% to compensate for the difference in the initial portion of the stress-strain curves. Points *a*–*g* indicate stress conditions where UT observations were carried out. Point *p* represents the peak stress, at which the laboratory test was stopped. The dashed blue curve represents the post-peak stage of the simulation. (For interpretation of the references to colour in this figure legend, the reader is referred to the web version of this article.)

(i.e. 0 MPa) values at 120 MPa. On the other hand, the averaged velocity parallel to the loading direction, $v_a^{\parallel}$, kept increasing with increasing compressional stress, and reached ~5300 m/s at 120 MPa. The difference of averaged velocity in different directions, quantified by the velocity anisotropy (k) that is calculated using the maximum, minimum, and mean values of v_a (i.e., v_a^{max}, v_a^{min}, and v_a^{mean}): $k = [(v_a^{max} - v_a^{min})/v_a^{mean}] \times 100\%$ (Babuška, 1984; Kern, 1993). k increased from 10% to 36% when the axial stress increased from 0 to 120 MPa. Moreover, from 0 to 80 MPa, k increased in a logarithmic fashion and the rate of change decreased gradually; whereas, from 80 MPa to 120 MPa, k increased linearly at a higher rate of change.

The initial velocity values of the iterative inversion, obtained by a linear fitting of travel time and distances between all source-receiver pairs at stress points *a*–*g* were 4476 m/s, 4599 m/s, 4716 m/s, 4891 m/s, 4814 m/s, 4815 m/s, and 4702 m/s, respectively (e.g. Fig. 4a and d).

Tomography results showed that velocity of the sample at 0 MPa was relatively uniform and consistent with the averaged velocity (Fig. 6a). As the stress increased to 20 MPa, small areas with increased and decreased velocities started to develop (Fig. 6b). In fact, two low velocity areas (< 4500 m/s) developed at the north-east and south-west parts of the sample, while the remaining parts had slightly increased velocity (> 4500 m/s). The size of this high velocity zone was relatively unchanged between 20 and 60 MPa; however, the velocity in this area increased consistently (Fig. 6b–d). From 80 to 100 MPa, the size of the high velocity zone shrank towards the centre of the sample (Fig. 6e–f). At 120 MPa, the low velocity zones were enlarged with further deceased velocity, and the high velocity zone shrank to the north-middle part of the sample (Fig. 6g).

3.3. Simulated AE and quantitative analysis

Comparison of the simulated AE against the mechanical behaviour (Fig. 7) shows that the first AE occurred at ~40 MPa (point *c*) and very few events were generated prior to 60 MPa (point *d*). From 60 to 100 MPa (point *d*–*f*), AE occurred at a relatively stable rate (~50 events per interval). Between 100 MPa and the peak stress point (point *f*–*p*), AE rate increased quickly to 150 events per interval. Finally, after the peak stress point (point *p*–*h*), the AE rate increased rapidly to 530, suggesting an exponentially increased AE rate. The variation of AE rate suggested that the crack initiation stage occurred at approximately 60 MPa, and the unstable cracking stage started at approximately 100 MPa (Martin, 1993).

For the complete AE event catalogue, we obtained a M_c of −6.6 and an overall b-value of 0.82 ± 0.09. This M_c value was used in the sliding time window method to evaluate the time variation of b-value as a function of time. In general, b-value decreases throughout the deformation of the specimen (Fig. 7), from an initial value of 1.3 at ~100 MPa to 0.8 at 130 MPa. From 130 MPa to the peak stress point, b-value recovered to 1 at the peak (point *p*). After the peak point, b-value rapidly dropped to 0.7.

To further investigate the significant change of AE behaviour before and after the peak stress point, we divided AE activities into pre-peak and post-peak stages and examined their spatial distribution and failure mode separately (Fig. 8). The majority of the AE occurred in the pre-peak stage were in tensile failure mode, evenly distributed throughout the sample, and sub-vertically oriented (Fig. 8a). Event density at this stage was < 5 counts/grid throughout the sample. AE occurred in the post-peak stage were mainly shear events localized along a shear band oriented approximately 70° with respect to the horizontal direction (Fig. 8b). Event density on the shear band was > 10 counts/grid, while the remaining parts of the sample were relatively quiescent with few AE recorded. Comparing the simulated fracture pattern with the compression test result, the inclined throughout fracture was successfully reproduced by the simulation (Fig. 8c).

4. Discussion

4.1. Damage process characterized by wave velocity and simulated AE

The variation of velocity is related to the change in elastic modulus at macroscopic scale, while the AE is associated with the degree of damage at microscopic scale (Diederichs et al., 2004; Lockner, 1993; Nur and Simmons, 1969). Combining the two provides detailed insight into the deformation and failure processes of the brittle rock.

The influence of closure of pre-existing microcracks on the elastic properties of the rocks was suggested almost one hundred years ago in the seminal work by Adams and Williamson (1923). Later laboratory studies observed that this effect causes velocity anisotropy with seismic waves traveling faster in the direction of the applied stress (Nur and Simmons, 1969; Tocher, 1957). In this study, we characterized the wave velocity difference in the directions parallel and perpendicular to the loading direction using velocity anisotropy (k). On the other hand, velocity difference between different regions of the sample was described using velocity heterogeneity.

The increases of $v_a^{\perp}$ and $v_a^{\parallel}$ with increasing axial stress prior to 60 MPa was related to the closing of pre-existing microcracks. The UT observations not only captured the increase of the averaged velocities, but also provided details of the velocity heterogeneity in the sample. The velocity heterogeneity, observed as high and low velocity zones, may have two origins: (1) heterogeneity of the mineral phases and microcracks in the rock sample and (2) end effect between the sample and platens stemming from the relatively high friction between them.

After 60 MPa, $v_a^{\parallel}$ kept increasing with increasing axial stress, but $v_a^{\perp}$ started to decrease, causing k to increase. This suggests that new microcracks were developing in preferred orientations and failure modes, and they had a more significant impact on the elastic modulus in the lateral direction than in the vertical direction. This interpretation was confirmed by the numerical simulation: most AE events occurred during this period were oriented in conjugate sub-vertical directions and in tensile failure mode. These AE events (i.e., microcracking) divided the sample into high and low velocity regions. As the damage accumulated and covered more regions of the sample, the areas of the high velocity zones decreased and the areas of the low velocity zones enlarged, causing more significant velocity heterogeneity.

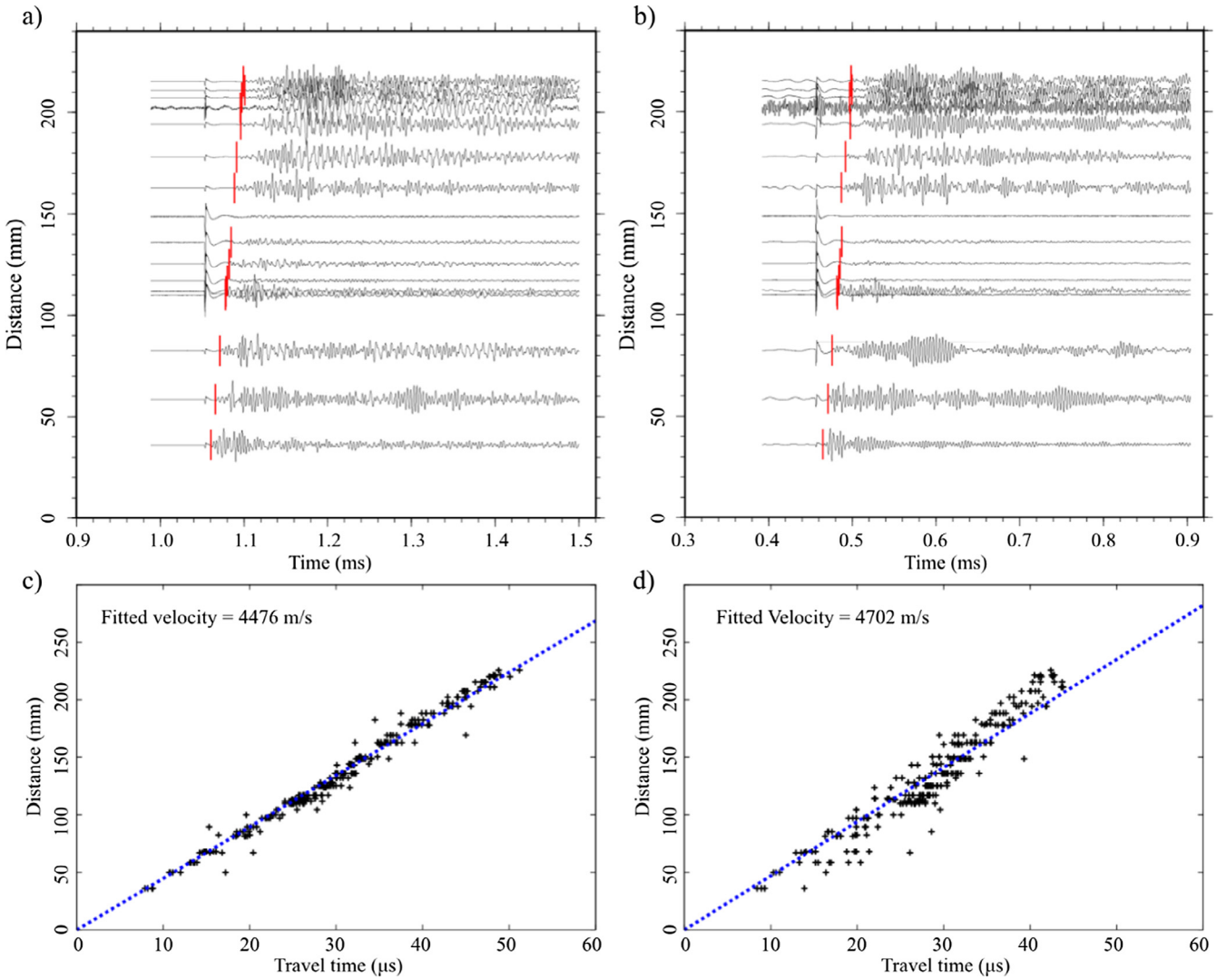

Fig. 4. Waveforms recorded by transducers 11–26 (from top to bottom) at the first stage of the UT test under (a) 0 MPa and (b) 120 MPa axial stress. Red bars indicate the manually picked P-wave arrivals. Note that due to the crosstalk between circuits, a wiggle appears at the beginning of each trace; although considered noise in most applications, it indicates the "zero" for wave travel time. (c) and (d) are P-wave velocities estimated from arrival pickings by simple linear fittings at 0 MPa and 120 MPa, respectively. (For interpretation of the references to colour in this figure legend, the reader is referred to the web version of this article.)

Velocity anisotropy has been suggested to be meaningful to rock burst prediction (Tocher, 1957). The observed k variation as a function of loading path resembles other laboratory studies (Goodfellow et al., 2014), and by comparing it with the stress-strain relation and simulated AE (Fig. 7), we were able to obtain a better understanding of the origin and development of the velocity anisotropy.

Upon 120 MPa, $v_a^{\parallel}$ kept increasing up to this point, even though fractures developed extensively under high stress. The reason for this behaviour may be twofold: first, fractures opened less in the direction paralleled than perpendicular to the loading direction, thus, had less influence on velocity; second, the raypaths between transducer pairs used for $v_a^{\parallel}$ measurements (i.e., between 12 and 24, 25, or 26) covered more high velocity zones than low velocity zones (Fig. 6).

The numerical simulation has successfully explained the tomography results up to 120 MPa. The designed UT observation would occur at 140 MPa; however, the sample failed abruptly at 136 MPa. Therefore, the last UT observation was done at 120 MPa, and after this point, laboratory observations were limited and our interpretation relied on the numerical simulation. As the axial stress continued to increase, the shear band became evident. After the peak stress, shear dominant cracking and the linkage between them became the major mechanism of crack interaction (Lei et al., 2000). The throughout fault that failed the sample, observed in the laboratory test and the simulation, verified such interpretation (Figs. 6g and 8c).

4.2. Rock failure precursors

Several potential precursors of the catastrophic failure of the rock were identified: (1) decrease of the averaged wave velocity in the direction perpendicular to loading, (2) increase of the heterogeneity and anisotropy of elastic wave velocity, (3) exponential increase of AE rate, (4) spatial localization of damage onto the failure plane, (5) an increase of the dominance of shear failure, and (6) slight recovery of b-value, followed by a significant drop.

The decrease of the average velocity (indicator 1) suggests that significant amount of damage has occurred resulting in a reduction in the apparent elastic modulus of the rock sample. As the damage continued to accumulate and new microcracks formed, high and low velocity zones developed with the increase of elastic wave velocity anisotropy (indicator 2). Our study suggested that indicators 1 and 2 may appear at approximately 45% (i.e. 60 MPa) and 60% (i.e. 80 MPa) of the compressive strength of the rock, respectively, providing meaningful hints for intermediate- to long-term prediction of rock failure.

At the unstable cracking stage, damage accumulates rapidly along

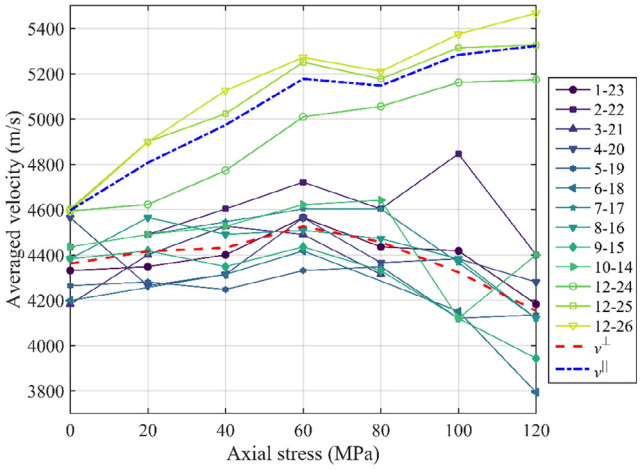

Fig. 5. Averaged P-wave velocity measurement from source and receiver pairs across the sample laterally (solid markers) and vertically (hollow markers). The averaged values of these velocities at different stress levels, calculated using transducer pairs at the same orientation, are represented by $v^{\perp}$ (blue dash-dot curve) and $v^{\parallel}$ (red dash curve), respectively. (For interpretation of the references to colour in this figure legend, the reader is referred to the web version of this article.)

the shear band (indicators 3, 4 and 5). These indicators became evident after 80% of the compressive strength of the rock (i.e. 100 MPa), and as the microcracks started to grow and coalescence, the throughout fault that catastrophically failed the rock sample formed quickly (Cai et al., 2004; Diederichs et al., 2004). Therefore, indicators 3, 4 and 5 may be considered as short-term prediction parameters.

b-value may assist intermediate- to long-term prediction of earthquakes as it gradually decreases along the failure process. However, the slight recovery before the catastrophic failure and significant drop right after (indicator 6) was more evident, making it a useful short-term prediction tool. The gradual decrease, slight recovery, and rapid drop of b-value before a large seismic event has been suggested by the work of Main et al. (1989) based on fracture mechanics, and it was in agreement with laboratory and field earthquake studies (Imoto, 1991; Lockner et al., 1991; Main et al., 1989; Weeks et al., 1978).

Other failure indicators were also suggested by researchers, such as increasing energy release rate, increase in spatial correlation length, and increase in scattering attenuation (Lei and Satoh, 2007; Main et al., 1989). These failure indicators, in addition to the indicators we identified, are closely related, and each of these aspects may have complicated evolution due to the heterogeneity of the rock. Therefore, it is important to integrate the analysis of several parameters to successfully predict rock failure.

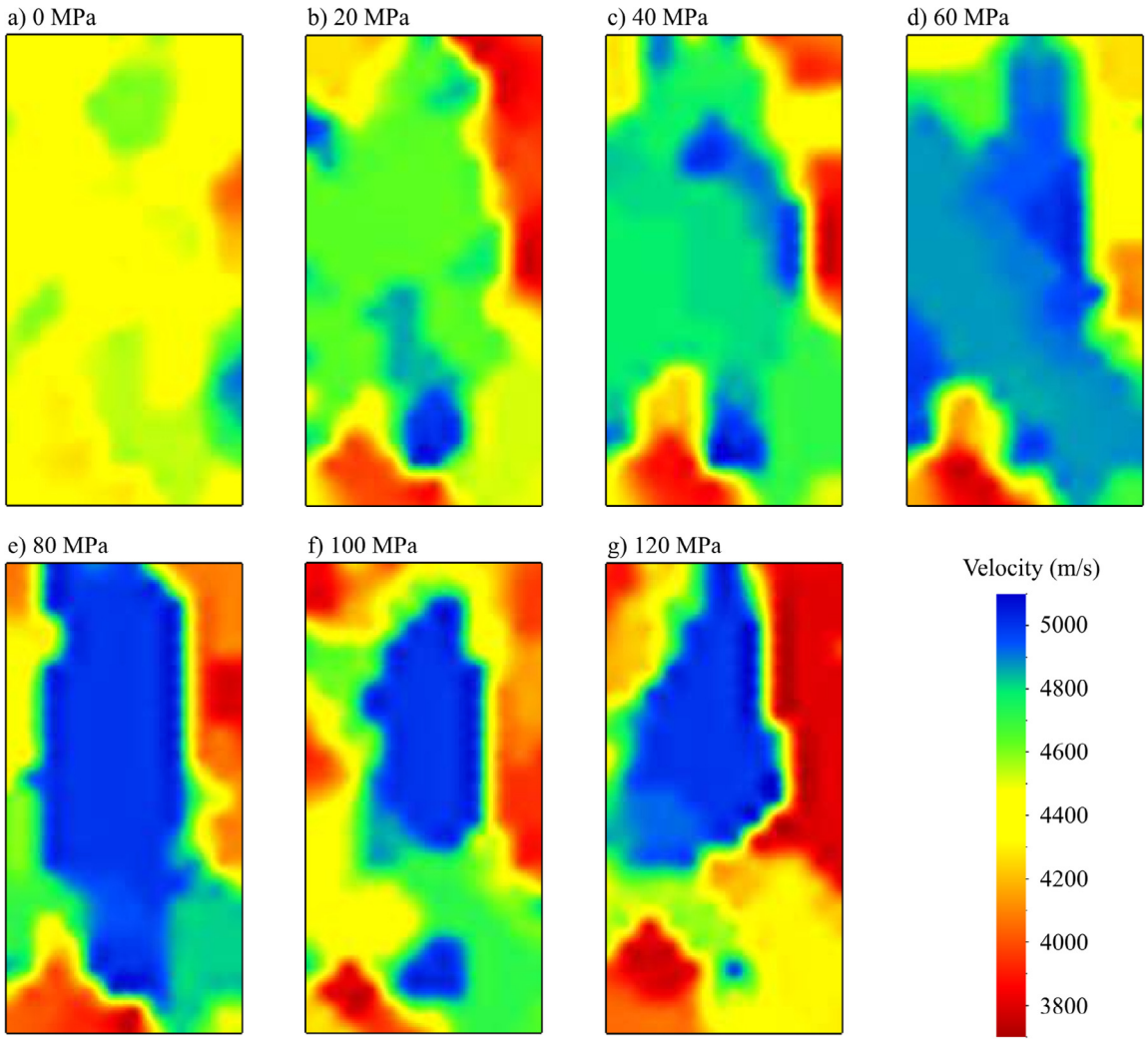

Fig. 6. UT velocity inversion results. (a)–(g) correspond to UT observations conducted at stress conditions 0, 20, 40, 60, 80, 100, and 120 MPa, respectively.

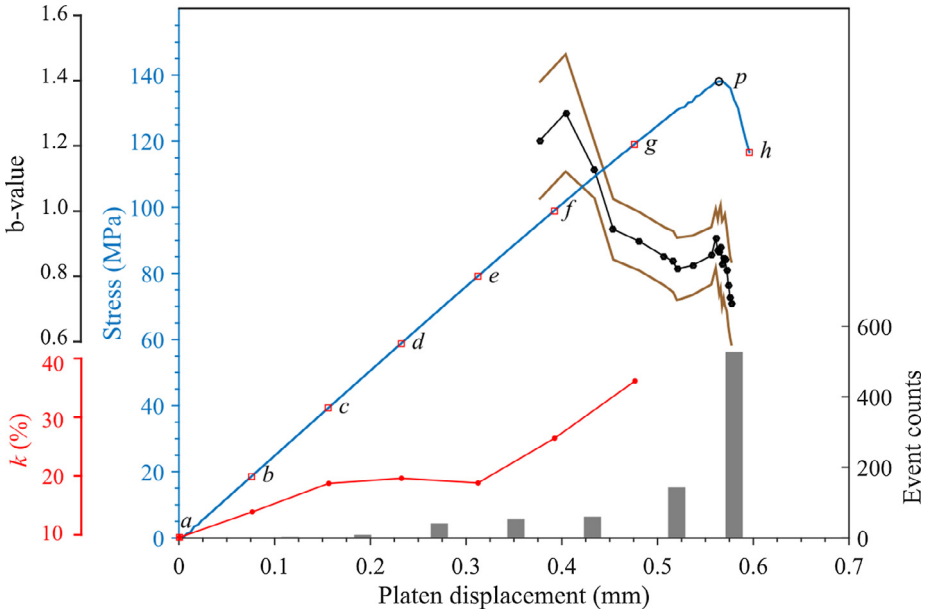

Fig. 7. Simulated axial stress (blue curve), non-cumulative AE event counts (columns), b-value (black curve) and velocity anisotropy (red curve) examined against the loading history. Note that in order to avoid the overlapping strain after peak stress, we use platen displacement as the horizontal axis. Brown lines indicate the errors associated with the b-values. Points *a–g* (red squares) correspond to stress points at 20 MPa intervals, *h* is the failure point. Peak stress point (*p*) is marked by the black hollow circle. (For interpretation of the references to colour in this figure legend, the reader is referred to the web version of this article.)

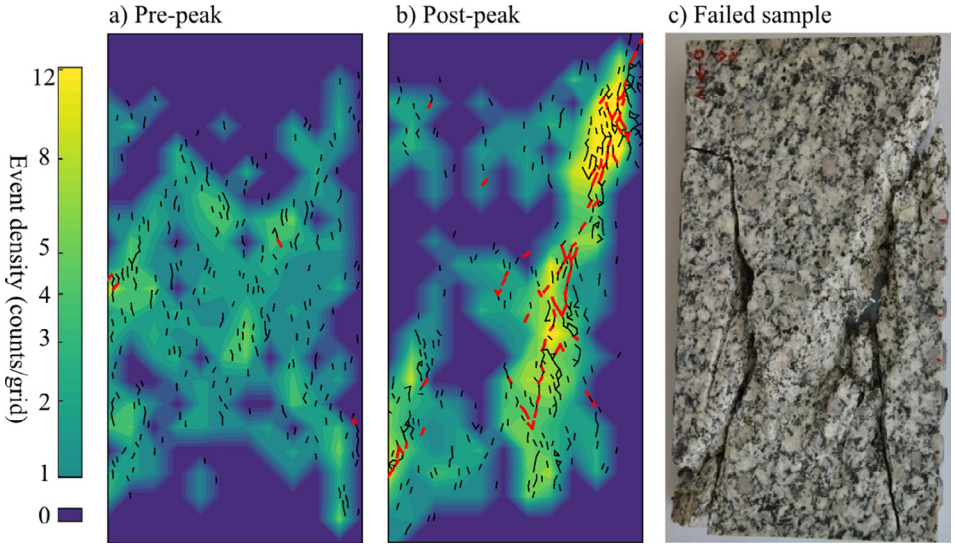

Fig. 8. (a) and (b) show the location and failure mode of simulated microcracks (i.e., AE) occurred pre- and post-peak, respectively, overlapping their spatial density maps. Density maps are in log scale for better illustration. Tensile dominant cracks are marked by thin black dashes and shear dominant cracks are marked by thick red dashes. (c) The tested rock specimen after the abrupt failure. Note the similarity in macroscopic fracture pattern between (b) and (c). (For interpretation of the references to colour in this figure legend, the reader is referred to the web version of this article.)

5. Conclusion

In this study, we employed ultrasonic tomography observations and FDEM numerical simulation method to investigate the progressive failure process of a rock sample under uniaxial compression. Six precursors related to critical behaviours prior to rock failure were identified, and they are comparable to published results. These precursory behaviours may also be obtained from field monitoring, for example, from seismic monitoring, and with the support of carefully calibrated numerical models, they have the potential in improving the accuracy of stability assessment of underground structures. In addition, these observations may also be useful to the forecast of mining and tunnelling induced seismicity. In future studies, the combination of technologies can be further developed by (1) recording induced AE during the compression test, (2) taking wave waveform information and attenuation into account to enhance the tomography results, and (3) using validated numerical models to simulate field scale problems.

Acknowledgement

This work has been supported through the NSERC Discovery Grants 341275 & 72031326, CFI-LOF Grants 18285 & 12911, Carbon Management Canada (CMC), Energi simulation, and the Special Fund for Basic Scientific Research IGPCEA (No. DQJB13B06), China. T.-M. He and Q. Zhao would like to thank Dr. Qinya Liu at the University of Toronto for her help in ultrasonic tomography.

References

Adams, L.H., Williamson, E.D., 1923. On the compressibility of minerals and rocks at high pressures. J. Franklin Inst. 195, 475–529.
Aki, K., 1965. Maximum likelihood estimate of b in the formula logN = a-bM and its confidence limits. Bull. Earthq. Res. Inst. Tokyo Univ. 43, 237–239.
Aki, K., Lee, W.H.K., 1976. Determination of three-dimensional velocity anomalies under a seismic array using first P arrival times from local earthquakes: 1. A homogeneous initial model. J. Geophys. Res. 81, 4381–4399.
Babuška, V., 1984. P-wave velocity anisotropy in crystalline rocks. Geophys. J. Int. 76, 113–119.
Barenblatt, G.I., 1962. The mathematical theory of equilibrium cracks in brittle fracture. Adv. Appl. Mech. 7, 104.
Bender, B., 1983. Maximum-likelihood estimation of B-values for magnitude grouped data. Bull. Seismol. Soc. Am. 73, 831–851.
Cai, M., Kaiser, P.K., Tasaka, Y., Maejima, T., Morioka, H., Minami, M., 2004. Generalized crack initiation and crack damage stress thresholds of brittle rock masses near underground excavations. Int. J. Rock Mech. Min. Sci. 41, 833–847.
Chang, S.-H., Lee, C.-I., 2004. Estimation of cracking and damage mechanisms in rock

under triaxial compression by moment tensor analysis of acoustic emission. Int. J. Rock Mech. Min. Sci. 41, 1069–1086.
Diederichs, M.S., Kaiser, P.K., Eberhardt, E., 2004. Damage initiation and propagation in hard rock during tunnelling and the influence of near-face stress rotation. Int. J. Rock Mech. Min. Sci. 41, 785–812.
Dugdale, D.S., 1960. Yielding of steel sheets containing slits. J. Mech. Phys. Solids 8, 100–104. http://dx.doi.org/10.1016/0022-5096(60)90013-2.
Efron, B., Tibshirani, R., 1986. Bootstrap methods for standard errors, confidence intervals, and other measures of statistical accuracy. Stat. Sci. 54–75.
Falls, S.D., Young, R.P., Carlson, S.R., 1992. Ultrasonic tomography and acoustic emission in hydraulically fractured Lac du Bonnet grey granite. J. Geophys. Res. Solid Earth 97, 6867–6884.
Falls, S.D.S., Young, R.P., 1998. Acoustic emission and ultrasonic-velocity methods used to characterise the excavation disturbance associated with deep tunnels in hard rock. Tectonophysics 289, 1–15. http://dx.doi.org/10.1016/S0040-1951(97)00303-X.
Goodfellow, S.D., Flynn, J.W., Reyes-Montes, J.M., Nasseri, M.H.B., Young, R.P., 2014. Acquisition of complete acoustic emission amplitude records during rock fracture experiments. J. Acoust Emiss. 32.
Greenleaf, J.F., Johnson, S.A., Lee, S.L., Hermant, G.T., 1974. Algebraic Reconstruction of Spatial Distributions of Acoustic Absorption within Tissue from Their Two-dimensional Acoustic Projections, Acoustical Holography. Springer.
Gutenberg, B., Richter, C.F., 1944. Frequency of earthquakes in California. Bull. Seismol. Soc. Am. 34, 185–188.
Hazzard, J.F., Young, R.P., Maxwell, S.C., 2000. Micromechanical modeling of cracking and failure in brittle rocks. J. Geophys. Res. Solid Earth 105, 16683–16697.
Hengxing, L., Derek, M.C., Bo, H., 2010. Effect of heterogeneity of brittle rock on micromechanical extensile behavior during compression loading. J. Geophys. Res. Solid Earth 115. http://dx.doi.org/10.1029/2009JB006496.
Imoto, M., 1991. Changes in the magnitude-frequency b-value prior to large (M ≥ 6.0) earthquakes in Japan. Tectonophysics 193, 311–325. http://dx.doi.org/10.1016/0040-1951(91)90340-X.
Jansen, D., Carlson, S., Young, R.P., 1993. Ultrasonic imaging and acoustic emission monitoring of thermally induced microcracks in Lac du Bonnet granite. Res. Solid Earth.
Johnston, D.H., Toksöz, M.N., 1980. Ultrasonic P and S wave attenuation in dry and saturated rocks under pressure. J. Geophys. Res. Solid Earth 85, 925–936.
Kern, H., 1993. P-and S-wave anisotropy and shear-wave splitting at pressure and temperature in possible mantle rocks and their relation to the rock fabric. Phys. Earth Planet. Inter. 78, 245–256.
Lei, X., Kusunose, K., Rao, M.V.M.S., Nishizawa, O., Satoh, T., 2000. Quasi-static fault growth and cracking in homogeneous brittle rock under triaxial compression using acoustic emission monitoring. J. Geophys. Res. Solid Earth 105, 6127–6139.
Lei, X., Satoh, T., 2007. Indicators of critical point behavior prior to rock failure inferred from pre-failure damage. Tectonophysics 431, 97–111.
Lisjak, A., Liu, Q., Zhao, Q., Mahabadi, O.K., Grasselli, G., 2013. Numerical simulation of acoustic emission in brittle rocks by two-dimensional finite-discrete element analysis. Geophys. J. Int. 195, 423–443.
Lockner, D.A., 1993. The role of acoustic-emission in the study of rock fracture. Int. J. Rock Mech. Min. Sci. Geomech. Abstr. 30, 883–899.
Lockner, D.A., Byerlee, J., Kuksenko, V., Ponomarev, A., Sidorin, A., 1991. Quasi-static fault growth and shear fracture energy in granite. Nature 350, 39–42.
Lockner, D.A., Walsh, J.B., Byerlee, J.D., 1977. Changes in seismic velocity and attenuation during deformation of granite. J. Geophys. Res. 82, 5374–5378.
Mahabadi, O.K., 2012. Investigating the Influence of Micro-scale Heterogeneity and Microstructure on the Failure and Mechanical Behaviour of Geomaterials. University of Toronto.
Mahabadi, O.K., Lisjak, A., Munjiza, A., Grasselli, G., 2012a. Y-Geo: a new combined finite-discrete element numerical code for geomechanical applications. Int. J. Geomech. 1, 153.
Mahabadi, O.K., Randall, N.X., Zong, Z., Grasselli, G., 2012b. A novel approach for micro-scale characterization and modeling of geomaterials incorporating actual material heterogeneity. Geophys. Res. Lett. 39. http://dx.doi.org/10.1029/2011gl050411.
Mahabadi, O.K., Tatone, B.S.A., Grasselli, G., 2014. Influence of microscale heterogeneity and microstructure on the tensile behavior of crystalline rocks. J. Geophys. Res. Solid Earth 119, 5324–5341.
Main, I.G., Meredith, P.G., Jones, C., 1989. A reinterpretation of the precursory seismic b-value anomaly from fracture mechanics. Geophys. J. Int. 96, 131–138.
Martin, C.D., 1993. The Strength of Massive Lac du Bonnet Granite around Underground Openings. University of Manitoba.
Mavko, G., Mukerji, T., Dvorkin, J., 1998. The Rock Physics Handbook: Tools for Seismic Analysis in. Porous Media.
Meglis, I.L.I.L., Chow, T., Martin, C.C.D., Young, R.P., 2005. Assessing in situ microcrack damage using ultrasonic velocity tomography 42, 25–34.
Munjiza, A., 2004. The Combined Finite-Discrete Element Method. John Wiley Sons Ltd.
Neumann-Denzau, G., Behrens, J., 1984. Inversion of seismic data using tomographical reconstruction techniques for investigations of laterally inhomogeneous media. Geophys. J. Int. 79, 305–315.
Nuannin, P., Kulhanek, O., 2005. Spatial and temporal b value anomalies preceding the devastating off coast of NW Sumatra earthquake of December 26, 2004. Geophys. Res. 32.
Nur, A., Simmons, G., 1969. Stress-induced velocity anisotropy in rock: an experimental study. J. Geophys. Res. 74, 6667–6674.
Paige, C.C., Saunders, M.A., 1982. LSQR: An algorithm for sparse linear equations and sparse least squares. ACM Trans. Math. Softw. 8, 43–71.
Paterson, M.S., Wong, T.-f., 2005. Experimental Rock Deformation: The Brittle Field. Springer.
Sayers, C.M., Kachanov, M., 1995. Microcrack-induced elastic wave anisotropy of brittle rocks. J. Geophys. Res. Solid Earth 100, 4149–4156.
Stanchits, S., Vinciguerra, S., Dresen, G., 2006. Ultrasonic velocities, acoustic emission characteristics and crack damage of basalt and granite. Pure Appl. Geophys. 163, 975–994.
Tatone, B.S.A., Grasselli, G., 2015. A calibration procedure for two-dimensional laboratory-scale hybrid finite–discrete element simulations. Int. J. Rock Mech. Min. Sci. 75, 56–72.
Tocher, D., 1957. Anisotropy in rocks under simple compression. Eos. Trans. Am. Geophys. Union 38, 89–94.
Weeks, J., Lockner, D.A., Byerlee, J., 1978. Change in b-values during movement on cut surfaces in granite. Bull. Seismol. Soc. Am. 68, 333–341.
Wiemer, S., Wyss, M., 2000. Minimum magnitude of completeness in earthquake catalogs: examples from Alaska, the western United States, and Japan. Bull. Seismol. Soc. Am. 90, 859–869.
Zhao, D., Hasegawa, A., Horiuchi, S., 1992. Tomographic imaging of P and S wave velocity structure beneath northeastern Japan. J. Geophys. Res. Solid Earth 97, 19909–19928.
Zhao, Q., 2017. Investigating Brittle Rock Failure and Associated Seismicity Using Laboratory Experiments and Numerical Simulations. University of Toronto.
Zhao, Q., Lisjak, A., Mahabadi, O.K., Liu, Q., Grasselli, G., 2014. Numerical simulation of hydraulic fracturing and associated microseismicity using finite-discrete element method. J. Rock Mech. Geotech. Eng. 6, 574–581. http://dx.doi.org/10.1016/j.jrmge.2014.10.003.
Zhao, Q., Tisato, N., Grasselli, G., Mahabadi, O.K., Lisjak, A., Liu, Q., 2015. Influence of in situ stress variations on acoustic emissions: a numerical study. Geophys. J. Int. 203, 1246–1252.
Zhu, W.C., Tang, C.A., 2004. Micromechanical model for simulating the fracture process of rock. Rock Mech. Rock Eng. 37, 25–56. http://dx.doi.org/10.1007/s00603-003-0014-z.